Estimating Void Nucleation Statistics in Laser-Driven Spall

Article *in* Journal of Dynamic Behavior of Materials · June 2020

DOI: 10.1007/s40870-020-00248-6

CITATIONS
3

READS
133

4 authors, including:

Debjoy Mallick
Army Research Laboratory
14 PUBLICATIONS **102** CITATIONS
SEE PROFILE

K.T. Ramesh
Johns Hopkins University
361 PUBLICATIONS **13,721** CITATIONS
SEE PROFILE

Journal of Dynamic Behavior of Materials
https://doi.org/10.1007/s40870-020-00248-6

RESEARCH PAPER

Estimating Void Nucleation Statistics in Laser-Driven Spall

D. D. Mallick[1,4] · J. Parker[2,4,5] · J. W. Wilkerson[3] · K. T. Ramesh[4,5]

Received: 7 March 2020 / Accepted: 29 May 2020

Abstract
We examine the statistical distribution of critical nucleation pressures necessary to dynamically grow voids during the spall failure of an AZ31B magnesium alloy. The approach uses laser-driven micro-flyers to generate spall over times of the order of tens of nanoseconds, allowing us to focus on void nucleation processes rather than void coalescence processes. Our methodology combines quantitative postmortem characterization of void mediated failure with time-resolved interferometry of the failure event, and reveals the dynamics of the failure process. We infer the distribution of the underlying nucleation pressures and explore the associated strain rate dependence of spall strength in these alloys.

Keywords Spall failure · Void nucleation and growth · Micro computed tomography · Photon doppler velocimetry · AZ31B Mg alloy · Laser-driven micro-flyer plates

Introduction

Spall failure occurs in a material under high-rate loading conditions where stress waves interact to create localized high tensile stresses, activating failure mechanisms such as dynamic void growth [1]. Improving the resistance of a material to the failure mechanisms associated with spall is then relevant to the goal of developing next-generation protection materials that must withstand ballistic or explosive loading. The role of dynamic void growth as a failure mechanism during spall has been a subject of study since Rinehart [2] characterized the ultimate tensile strength of steel, brass, Al, and Cu alloys under explosive loading. In dynamic void growth, the local dynamic hydrostatic tension causes the unstable nucleation and growth of a cavity [3, 4]. These cavities, or voids, coalesce to degrade the load-bearing capacity of the material.

This phenomenon is conventionally studied with gas guns and explosive loading, typically resulting in a single valued "spall strength". Such loading techniques can achieve strain rates as high as 10^7 s^{-1} or more, but can make specimen recovery difficult due to the large kinetic energies from loading. Instead, laser-driven approaches have been sparingly employed in recent spall studies to improve experimental throughput and impart less kinetic energy upon the specimen than through conventional experimental techniques [5–16]. Peralta et al. and Wayne et al. [11, 12] used the Trident laser facility at Los Alamos National Laboratory with the goal of causing "incipient" spallation in copper polycrystals. In incipient spall, the growing voids in the region of high tension (called the spall plane) have not coalesced to form a contiguous plane of failure in the specimen. Their approach used the laser facility to accelerate flyers for impact against the specimens, and they then performed optical and scanning-electron microscopy, along with electron backscattering diffraction, to identify the microstructure features that act as the void nucleation sites with greatest frequency (However, the sectioning and polishing methods used to uncover the voids for microscopy were destructive to the specimen).

Brown et al. [13–15] used the same laser-driven flyer system at the Trident laser facility, but used micro-computed-tomography (μ-CT) techniques to non-destructively

✉ D. D. Mallick
debjoy.d.mallick.civ@mail.mil

1 US Army CCDC Army Research Laboratory, 321 Colleran Road Aberdeen Proving Ground, Adelphi, MD 21005-5066, USA

2 US Army CCDC Soldier Center, Natick, MA 01760, USA

3 J. Mike Walker '66 Department of Mechanical Engineering, Texas A&M University, College Station, TX 77843, USA

4 Hopkins Extreme Materials Institute Johns Hopkins University, 140 Malone Hall, Baltimore, MD 21218, USA

5 Department of Mechanical Engineering, Johns Hopkins University, 223 Latrobe Hall, Baltimore, MD 21218, USA

Published online: 17 June 2020

obtain statistics of incipient spall voids within the specimen. They first examined void statistics in spall of polycrystalline copper, correlating the shape of captured voids to potential microstructure features where failure nucleates such as high-angle grain boundaries [13, 14]. Their findings were compared against numerical simulations incorporating crystal plasticity and void growth models with good agreement [17, 18]. Subsequently, they applied their approach to nickel and titanium polycrystals, finding that there may be potential thresholds in the statistics that can differentiate between when a void has just nucleated, grown, or coalesced [15]. We further investigate the utility of these postmortem statistics here.

Conventional spall strength evaluations rarely address these statistics of the dynamic failure threshold. Grady and Vogler et al. [19, 20] have identified significantly varied shock failure behavior within even individual shocked specimens, especially in the presence of diverse dissipative structures like materials with fine-grained microstructures. To better understand this stochasticity, we use a laser-driven micro-flyer apparatus [21] that imparts four orders of magnitude less kinetic energy into the specimen than conventional methods, while attaining similar or higher strain rates all on the lab-bench. The lower kinetic energy aids in specimen recovery for subsequent characterization. Analysis of the recovered specimen with micro-computed-tomography techniques reveals the pressure threshold statistics for unstable dynamic void growth that ultimately leads to spall failure in the specimen.

Material Investigated and Experimental Methods

Magnesium alloys are an attractive material system for protection applications owing to their high specific strength (the ratio of the yield strength to the density) and stiffness, but can have low failure strains relative to other lightweight structural metals (e.g. Al, Ti). Under dynamic conditions experienced by protection materials undergoing ballistic impact, magnesium has shown a relatively low resistance to cavitation-driven spall failure [22], however the advantageous specific strength continues to draw interest in impact applications where Mg has a tremendous weight savings potential for vehicle and personnel armor [23]. We examine dynamic void growth during the spall failure of AZ31B Mg alloy thin foils. The AZ31B Mg alloy thin foil targets are prepared using a shear-based deformation process called extrusion-machining that exploits large strains intrinsic to machining with the dimensional control of extrusion [24]. The 175 μm thick samples are processed to develop a nominal von Mises strain of 0.6 at a strain rate of 6×10^3 s^{-1}, resulting in a highly twinned and sheared microstructure with an average grain size of ~ 2.4 μm (by area fraction) and with a uniformly distributed grain size distribution with significant area fractions between 2 and 15 μm (Shown in Fig. 1). 3 mm diameter specimen disks are punched from the sample and are adhesively bonded to a 125 μm thick spacer that separates the specimen coupon from the flyer. The foils are characterized by tilted-basal type textures with the (0002) basal planes aligned at an angle with respect to the foil surface [24] (EBSD scans for these targets and experimental configuration are presented in detail in [21]).

The AZ31B Mg thin foils are subjected to shock loading using a laser-driven micro-flyer apparatus [21] which launches 50 μm thick and 1.5 mm diameter Al flyers at impact velocities up to 1.5 km/s to generate spall failure in the 175 μm thick AZ31B Mg targets. The spall response is characterized through analysis of the free-surface velocity history obtained with photon Doppler velocimetry (PDV) employing a probing spot size of ~ 50 μm, ensuring that the material response of multiple grains is captured during the experiment. Both the laser-driven micro-flyer apparatus and the velocimetry are described in detail by Mallick et al. [21, 25, 26] and were developed with assistance from the Dlott research group [27].

Results: Velocimetry and Microstructure Characterization

The PDV during the impact experiments provides a direct measurement of the free surface velocity of the AZ31B Mg alloy samples. The velocimetry result for the experiment that is the focus of this study is presented in Fig. 2. Note that the total time is only 80 nanoseconds. This velocimetry signature is the signature of a spall failure, where a piece of the target material

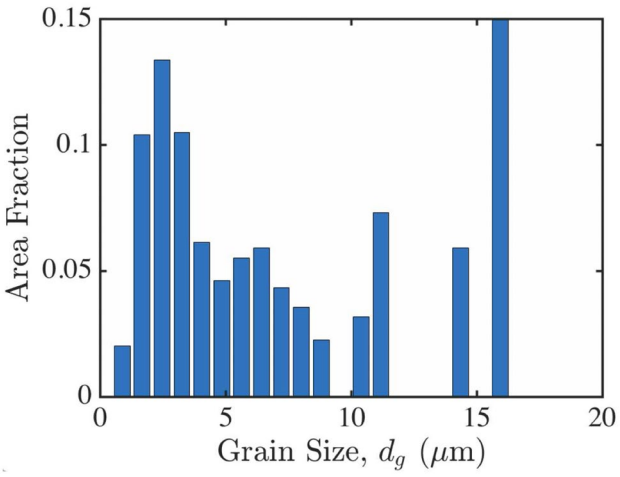

Fig. 1 Distribution of grain size d_g by area fraction in the as-received AZ31B thin foil

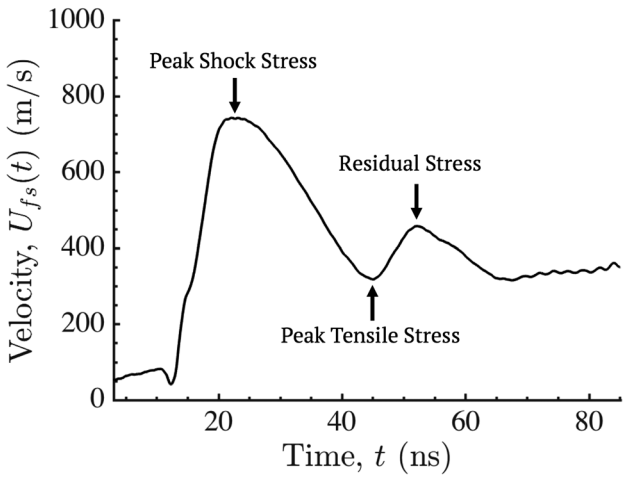

Fig. 2 Velocimetry record from presented spall experiment with peak compression/shock stress, peak tensile stress, and residual stress events labeled with arrows

begins to separate from the overall foil as a result of the process of spallation (failure under high dynamic tensile stress).

The free surface velocity history shown in Fig. 2 is analysed to understand the stress history in the target throughout the spall failure process (Experiment 1 in Table 1). At ~ 25 ns, the peak compressive stress is achieved, corresponding also to the maximum compressive hydrostatic stress, $\Sigma_{peak} \approx \frac{\sigma_{kk}}{3}$ (this is denoted by "Peak Shock Stress" in Fig. 2). The maximum velocity is defined as U_{max}, allowing an estimation of the peak shock stress as,

$$\Sigma_{peak} = -\frac{1}{2}\rho C_0 U_{max}, \tag{1}$$

with reference density ρ and bulk wave velocity $C_0 = \sqrt{K/\rho}$, where K is the bulk modulus, noting that the stress state is not purely hydrostatic but the yield and shear strengths of the material are small in comparison to the shock stress. In the experiment analyzed here, this peak shock stress is ~ −2.99 GPa, where the negative sign denotes compression. The velocity "pullback" signal occurs at ~ 45 ns (the point denoted by "Peak Tensile Stress" in Fig. 2), with the corresponding "pullback" velocity defined as $U_{max} - U_{min}$. The so-called "uncorrected" spall strength Σ^* of the material can then be estimated by

$$\Sigma^* = \frac{1}{2}\rho C_0 (U_{max} - U_{min}). \tag{2}$$

We perform a postmortem recovery analysis of a single spall experiment for this study by capturing the deformed specimen in a tray lined with polydimethylsiloxane that provides a soft catch, yet is optically transparent to allow for the PDV velocimetry. We also conducted four other spall experiments without recovery on the same AZ31B Mg alloy sample, measuring an average spall strength calculated using Eq. (2) of 1.69 ± 0.06 GPa (Table 1 also includes these 4 experiments performed without recovery). Figure 2 also shows the spall pulse corresponding to the residual stress in the separated spalled plate. The velocity corresponding to the "Residual Stress" is denoted by $U_{residual}$. This velocity approaches U_{max} in over-driven spall experiments, where the magnitude and duration of the tensile stresses nucleates and grows failure mechanisms to full coalescence in the spall plane [28]. In the case of the limited nucleation and growth of failure mechanisms due to the short shock duration and lower shock stress imposed by the laser-driven experiment in this work, there is a residual stress in the spall plane corresponding to Eq. (2), where $U_{residual}$ is substituted for U_{min} (i.e. $U_{residual} < U_{max}$ resulting in a residual tensile stress of ~ 1.15 GPa in this particular case) [29, 30].

The duration of tensile stress is estimated from Fig. 2 by determining the crossover point between compression to tension from Σ_{peak} to Σ^* using the difference in time between the two events in the velocity history (~ 19 ns in this case). The resulting tensile stress history is assumed to be monotonically increasing from 0 to 1.69 GPa over ~ 7 ns, effectively assuming a very rapid rise past the Hugoniot elastic limit [31] as the material moves from peak compression into peak tension. The velocity record indicates residual tensile stress of about ~ 1.15 GPa after peak tension, but the duration and variations in the residual history following the peak tension cannot be easily determined without a full simulation because the interaction between the residual stress wave and the partially separated spall plane is very complex.

Table 1 Summary of spall experiments performed with 175 µm thick AZ31B Mg alloy specimens, with an asterisk denoting the experiment performed with recovery for the subsequent postmortem XCT analysis

Test number	Shock Stress Σ_{peak} (GPa)	Pullback Velocity $U_{max} - U_{min}$ (m/s)	Spall Strength Σ^* (GPa)	Tensile Strain Rate $\frac{\dot{v}}{v_0}$ ($\times 10^6$ s^{-1})
1*	2.99	426	1.69	2.12
2	2.98	449	1.77	3.49
3	3.04	430	1.70	2.43
4	3.60	412	1.63	3.24
5	3.81	423	1.67	2.83

Now that we have an approximation for the stress state that caused the spall failure observed in Fig. 2, we examine the recovered sample to understand the consequences of that dynamic loading history. Figure 3a-c shows a couple of slices and a 3D reconstruction of the micro-computed tomography (μ-CT) scan of the deformed specimen corresponding to the velocity history shown in Fig. 2, taken with a Bruker Skyscan 1172 μ-CT (Kontich, Belgium) using a 0.81 μm^3 voxel size. The reconstructed μ-CT scan indicates the existence of a principal spall plane where voids are clustered. The spall plane consists of a ~ 1 mm diameter and ~ 20 μm thick region containing a collection of voids. Most of the void growth is along the principal spall plane, but the voids are not fully linked up, confirming that the spall failure was an incipient spallation as indicated by the residual stress in the velocity history after peak tensile stress. The reconstructed scan is segmented in MATLAB using Otsu thresholding. A morphological closing operation using a disk structuring element is performed to eliminate mis-classified pixels due to noise. The size of the structuring element is chosen by examining mean void radius from the segmented scan while changing the structuring element size. The structuring element is varied between 2 pixels and 5 pixels, and the smallest changes in mean void size with respect to changes in filter threshold occur with a structuring element size of 3 pixels.

The resulting dataset captures ~ 2500 voids, the sizes of which can be characterized from the μ-CT data. The average of the measured principal radii of each void is defined as the final radius a^{final}, and varies from 1 to 148 μm. The void aspect ratio (ratio of largest principal radius to smallest principal radius) varies from unity to 17.75 as shown in Fig. 4. Notice that the scan voxel size makes sub-micron voids impossible to resolve in this dataset. Some of the captured void data undoubtedly consists of individual voids that have impinged upon each other to create a coalesced void.

To identify individually grown voids, we first calculate the mean inter-void spacing in the dataset, l_{nn}. Voids with radii larger than half of this l_{nn} spacing are likely to be a coalescence of two or more voids, so we exclude voids with radii larger than $l_{nn}/2 = 6.85\,\mu m$. This threshold is illustrated as the solid purple line in Fig. 4, and eliminates ~ 175 voids from the μ-CT dataset. The aspect ratio, or shape, of void regions may also indicate multiple coalesced voids, so we leverage the simulations of [32], who consider plastic anisotropy and orientation-dependent activation of deformation mechanisms in pure Mg to estimate individual void aspect ratios under far field loading of various triaxialities. Their results indicate a maximum aspect ratio of 3.5 for a single deforming void, so we remove ~ 1100 voids from the μ-CT dataset with larger aspect ratios, identifying these as

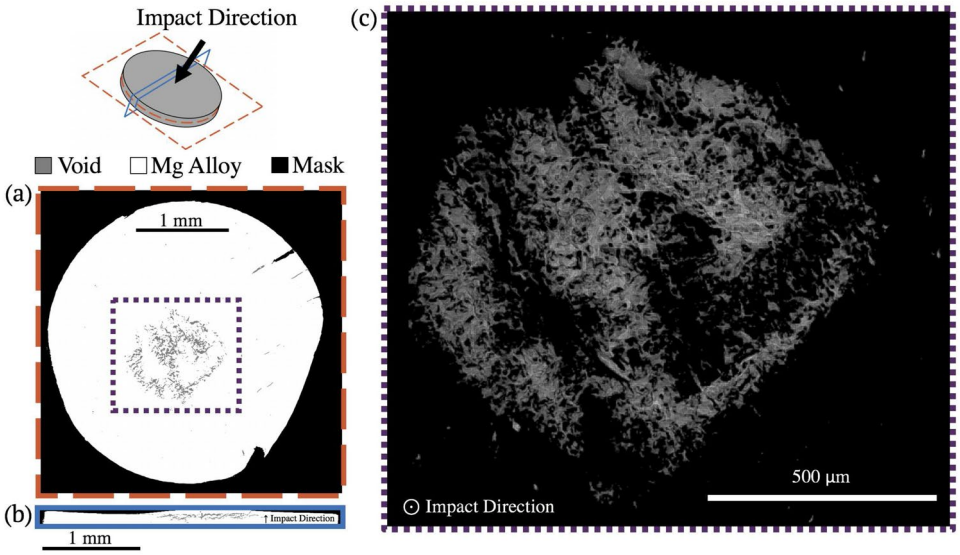

Fig. 3 XCT scans of the deformed specimen disk from Test Number 1. **a** XCT slice segmented to show voids (grey) in the AZ31B Mg alloy (white) after masking off regions outside the specimen (black). This slice is taken at a depth of approximately 145 μm into the specimen disk away from the impacted face, and shows the plane perpendicular to the direction of impact (cut plane shown in top schematic using dashed red lines). The damage region is emphasized by a purple dotted box. **b** Side slice of the specimen disk taken through the center of the disk (cut plane shown in top schematic using a blue solid line). **c** 3D reconstruction of voids in the spall plane, now with the AZ31B Mg alloy masked off as well (region of interest shown as dotted lines in **a**). Note the incipient to intermediate spall exhibited by regions of isolated voids and intermittent regions of coalesced voids

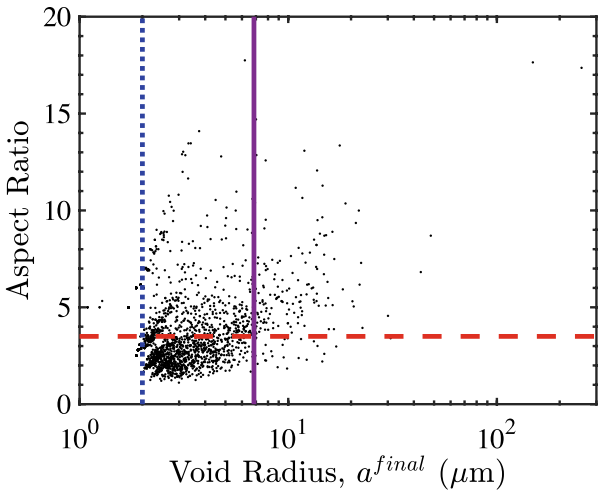

Fig. 4 Mean void radius and aspect ratio data from filtered μ-CT scan of deformed target. The void radius is the average of the principle radii of each void. A solid purple line is shown where data is excluded when void radii are above half the mean inter-void distance (a threshold of 6.85 μm). A dashed red line is shown where data is excluded above aspect ratios of 3.5. A dotted blue line is shown where data is excluded below the noise threshold void radii of 2 μm

likely to be coalesced voids (i.e., we ignore the data above the dashed red line in Fig. 4).

The empirical cumulative distribution of the void radii data for aspect ratios less than 3.5 is shown in Fig. 5 as the solid blue line. In the case of incipient spall, only some of the voids will have grown to a large radius, so we assume the resulting void radii follow a bounded power law distribution,

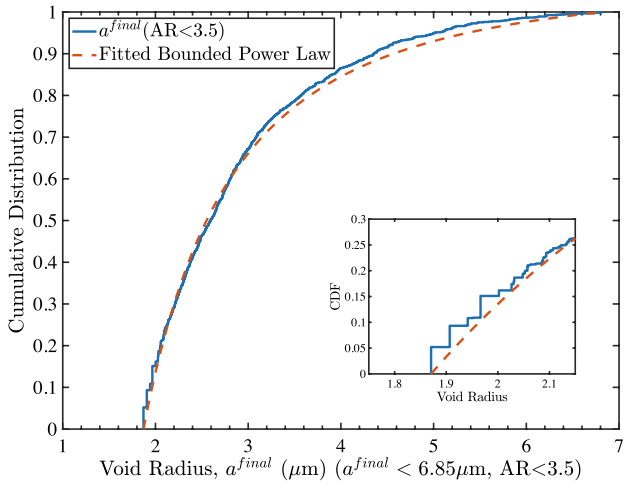

Fig. 5 Experimental cumulative distribution function of voids with void radii below 6.85 μm and aspect ratios less than 3.5 shown as the solid blue line. The dashed red line is the cumulative distribution of a fitted bounded power law distribution. The inset shows voids with radii < 2 μm are mixed with noise, so we exclude those voids as shown in Fig. 4 (blue dotted line)

$$g(a) = \beta \frac{a^{\beta-1}}{a_{max}^{\beta} - a_{min}^{\beta}}. \tag{3}$$

The cumulative distribution function is obtained as the integral of Equation 3, i.e. $G(a) = (a^{\beta} - a_{min}^{\beta})/(a_{max}^{\beta} - a_{min}^{\beta})$. The fitted power law distribution of Equation 3 is shown as the red dashed line in Fig. 5 with a power law shape parameter of $\beta = -2$. This fit shows excellent agreement with the experimentally observed void subset. The inset in Fig. 5 shows step-like data clustering for void radii smaller than 2 μm, suggesting that data under that threshold is mixed with noise from measurements near the μ-CT instrument resolution limit. Those ~ 150 voids are to the left of the dotted blue line in Fig. 4 and are excluded from the dataset going forward.

To quantify the error from using μ-CT data to obtain void radius statistics, we utilize the μ-CT shape error analysis by Patterson et al. [33]. Their experimental study shows an absolute error below 10 percent in measuring discernible axis lengths (Feret's diameter) in an object once the number of voxels in the object approaches ~ 1000 conservatively. To estimate the error based on void size in our study, we apply a least squares logarithmic fit of,

$$\epsilon = 0.3906 - 0.05386 \log(N_{vox}), \tag{4}$$

with absolute error percentage ϵ and number of voxels N_{vox} ($R^2 = 0.5281$). Now that we know both the tensile stress history and the resulting population of individual voids within the spall domain for this specimen, we can examine the nucleation and growth of voids during the spall process. We proceed with the subset of voids illustrated by the histogram in Fig. 6 selected by the aforementioned size and aspect ratio criteria. The error bars in Fig. 6 denote the changes

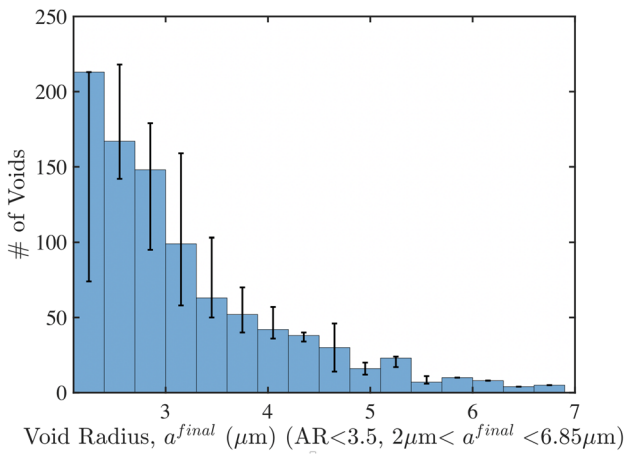

Fig. 6 Histogram of a subset of the void distribution from Fig. 4 containing only voids with radii between 2 and 6.85 μm, and aspect ratios below 3.5

in histogram counts if the absolute error from Eqn. (4) is applied to the entire dataset given fixed bin limits with lower errors associated with larger void sizes, as expected.

Discussion

Nucleation and Growth of the Weakest/Largest Void

The stability of single voids in elastic-plastic materials subjected to far-field hydrostatic tension has been discussed by a number of researchers such as Huang et al. [34] and Wu et al. [3]. Modeling the relationship between this instability and spall failure, separate from models of just the deformation mechanisms in this complex material system [35], involves the interactions of a number of voids with some size distribution and has been explored by Molinari and Wright [4] and Wright and Ramesh [36]. More recently, Wilkerson and co-workers have addressed the problem for ultra-high rate loading like in laser-driven experiments [37, 38]. Here we use an analytical result from Huang et al. [34], who developed an expression for the critical pressure $\mathcal{R}_y$ for void nucleation and unstable growth:

$$\mathcal{R}_y = \frac{2}{3}\sigma_y\left\{1 - \ln\frac{3}{2}\frac{\sigma_y}{E}\right\}. \tag{5}$$

Here, the Young's modulus is E and σ_y is the yield strength. To account for Hall–Petch strengthening, the yield strength may be modeled as $\sigma_y = \sigma_0 + k_y/\sqrt{d_g}$ where σ_0 is the Hall–Petch reference strength, k_y is the Hall–Petch strengthening constant, and the grain size is d_g. Using $\sigma_0 = 12.2$ MPa [39], $k_y = 7.2$ MPa $\cdot$ mm$^{1/2}$ [39] and $d_g = 2.4\,\mu$m [21], $\mathcal{R}_y = 0.64$ GPa for the AZ31B Mg alloy in this study. This strength is on the order of those inferred from shock experiments in similarly fine-grained Mg alloys loaded at comparable strain rates [40].

The evolution of void size under monotonically increasing far-field hydrostatic tension is described by a nonlinear ordinary differential equation, which can be solved analytically for the special case of a constant tensile strain rate [4, 38], giving the final void radius of an initially infinitesimal void as,

$$a^* = \sqrt{\frac{8}{33}}\frac{\left\langle \Sigma^* - \mathcal{R}_{cr}\right\rangle^{3/2}}{\sqrt{\rho}\dot{\Sigma}^*}. \tag{6}$$

The reference density is $\rho = 1773.75\,\mathrm{kg/m^3}$ [41] for the alloy in this study. After substituting the remaining parameters from the material properties and from the velocity record, ($\dot{\Sigma}^* = 2.46\times10^8$ GPa/s, $\Sigma^* = 1.69$ GPa) the resulting maximum void radius is $a^*_{max} = 1.702\,\mu$m when $\mathcal{R}_{cr}$ takes on its minimum value, $\mathcal{R}_{cr} = \mathcal{R}_y$. This maximum void radius is larger than nearly all of the raw void data, and nearly a third of the maximum of the void subset identified in the prior section, so we now consider post-spall void growth dynamics to gain further insight into the failure threshold of the AZ31B Mg alloy.

Estimating Statistical Distributions of Void Nucleation Pressures

Notice that Eq. (6) gives the void radius at the moment of peak tension a^*, but that our captured void radius statistics, for a^{final}, are from the recovered samples after any subsequent growth and potential post-spall loading. With that caveat, we examine the statistics of the void radius distribution to see if we can understand the extent of the difference between a^{final} and a^*. Wilkerson and Ramesh [42] consider the maximum possible pressure for lattice instability as the ideal tensile strength of the material, $\mathcal{R}_{eos} = \rho C_0^2/4S$ with S as the linear coefficient of the shock-velocity to particle–velocity relationship. For pure and alloyed magnesium, $S \approx 1.28$ [43], resulting in an estimate of the ideal strength as $\mathcal{R}_{eos} = 7.15$ GPa. In order to incorporate nucleation into a critical pressure threshold, they assume that the critical nucleation pressure $\mathcal{R}_{cr}$ at any random position in the material lies between $\mathcal{R}_y$ and $\mathcal{R}_{eos}$. The stochastic distribution of the critical pressures between $\mathcal{R}_y$ and $\mathcal{R}_{eos}$ is difficult to determine for a given material, so we attempt to characterize it henceforth, with the intuition that the largest voids will correspond to the lowest critical pressures, and vice versa.

In all likelihood, there is further void growth after spall because the velocity record indicates residual tension in the spall plane, so $a^{final} > a^*$. Even in the case of over-driven spall, there is a short transient of tension after peak tension as the coalescing failure relaxes stress in the spall plane, growing the voids so that $a^{final} > a^*$. We must consider the input void distribution when estimating the critical nucleation pressures. Wilkerson and Ramesh [37] have demonstrated that under a transitional void radius a^*_{trans}, void growth is limited by dislocation drag mediated resistance.

They present a closed form expression for $a^*_{trans} = \frac{3}{bN_mC_s}\sqrt{\frac{6}{11}\left\langle \Sigma^* - R_y\right\rangle}$ with Burgers vector $b = 0.321$ nm [39], mobile dislocation density $N_m = \sim 1 - 10\times10^{15}\mathrm{m}^{-2}$ [44], and shear wave speed $C_s = 3065$ m/s [41], resulting in a transitional void radius between 1.7 and 0.17 μm depending on the mobile dislocation density. When above this transitional void radius, void growth rates are controlled by inertial resistance. Inertia mediated void growth rates are uniform across initial void radii, implying that both $a^{final}_{min} = \Delta a + a^*_{min}$ and

$a_{max}^{final} = \Delta a + a_{max}^{*}$. This calculated radius threshold for uniform post-spall growth is below the minimum void radius in our experimental data, so we assume that the stochastic distribution of a^{final} is the same as the distribution of a^{*}.

As the largest void a_{max}^{final} corresponds to the lowest critical pressure $\mathcal{R}_{cr} = \mathcal{R}_{y}$, we take the ratio of a^{final} to a_{max}^{final} using Eqn. (6), and invert this ratio to obtain an expression for $\mathcal{R}_{cr}$,

$$\mathcal{R}_{cr} = \Sigma^{*} - \left\langle \Sigma^{*} - R_{y} \right\rangle \left(\frac{a^{final} - a_{min}^{final}}{a_{max}^{final} - a_{min}^{final}} \right)^{2/3}. \tag{7}$$

The probability density and empirical cumulative distribution of resulting nucleation pressures from this procedure are shown in Fig. 7a, b (solid blue) with an overlaid bounded power law fitted to the data (dashed red line). The experimental distribution begins at 0 and ends at Σ^{*}=1.69 GPa as expected. Error bars are calculated by substituting the dataset with the maximum and minimum error from Eqs. (4) into (7) while keeping the histogram bin limits constant. The fitted bounded power law $g(\mathcal{R}_{cr})$ follows the same analytical form of the probability density for a^{final} in Eq. (3) but with $\beta = 2$. The fitted power law follows the empirical distributions with reasonable agreement, except at the highest nucleation pressures near ~ 1.6 GPa corresponding to smaller void radii where errors in the μ-CT technique are the largest.

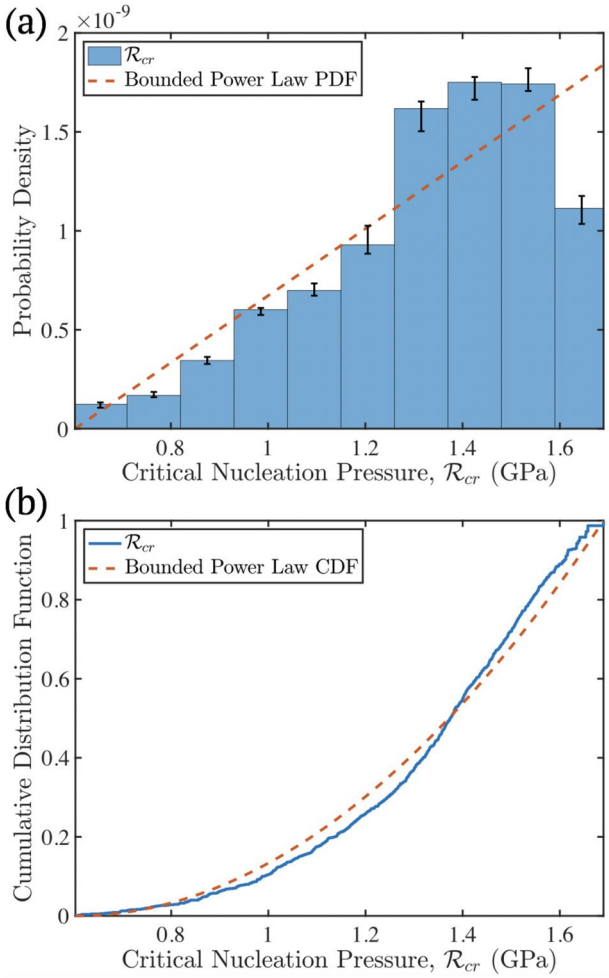

Fig. 7 **a** Probability distribution function of critical nucleation pressures $\mathcal{R}_{cr}$ calculated from observed void radii a^{final}. The dashed line is a bounded power law distribution fit. Error bars are calculated from the absolute errors in the void size distribution from Eq. (4). **b** Cumulative distribution function of critical nucleation pressures $\mathcal{R}_{cr}$ calculated from observed void radii a^{final}. The dashed line is a bounded power law distribution fit

Estimating Spall Strength from the Statistical Nucleation Pressures

Assuming that the shape of the nucleation pressure threshold distribution remains the same from Σ^{*} to $\mathcal{R}_{eos}$, an analytical model is applied to estimate spall strengths across various strain rates (see Wilkerson and Ramesh [42] for complete details),

$$\Sigma^{*} = \mathcal{R}_{y} + \frac{K}{\zeta}^{\beta+7/2} \sqrt{\frac{(\mathcal{R}_{eos} - \mathcal{R}_{y})^{\beta} \frac{\dot{v}}{v_0}}{\frac{4}{3}\pi (\frac{8}{33})^{\frac{3}{2}} C_0^3 K^{\beta} \xi N_v}} (\frac{\dot{v}}{v_0})^{\frac{2}{\beta+7/2}}, \tag{8}$$

with $\zeta = \frac{9+2\beta}{7+2\beta}$ and $\xi = (\beta + 9/2)2^{\beta}\Gamma(\beta)\prod_{i=1}^{\beta}(9+2i)^{-1}$. An alternative version of Eqn. (8) is also provided in [47]. The void number density N_v is estimated by looking at the mean void spacing l_{nn} in the raw void distribution by $N_v = 1/l_{nn}^3 \sim 3.9 \times 10^{14}$ m^3. A single standard deviation in

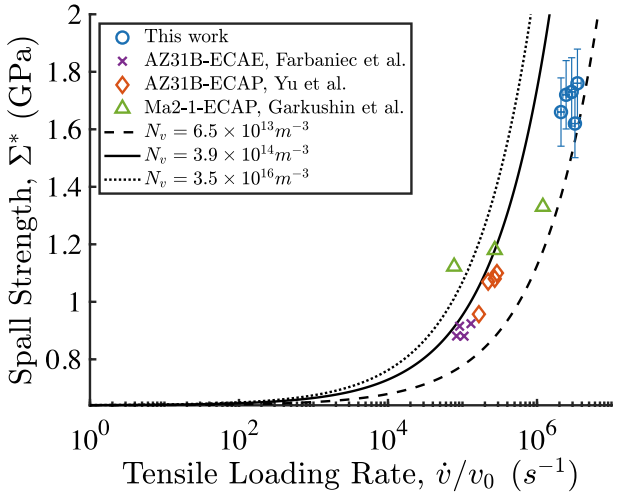

Fig. 8 Modeled trend in spall strength with respect to strain rate using three measured cavity number densities N_v, and the critical nucleation pressure probability density (black lines). Experimental spall strength measurements on similar Mg alloys are overlaid from [41, 45, 46]

the mean void spacing from the tomography data prescribes a wide range of N_v from 6.9×10^{13} m^{-3} to 3.5×10^{16} m^{-3}, so each bound and the mean is plotted as lines in Fig. 8. The model using the mean void spacing is shown as a solid black line, while the model using the void spacing decreased by a standard deviation is shown as a dashed black line, and the model using the void spacing increased by a standard deviation is shown as the dotted black line.

Farbaniec et al. [41] performed gas-gun spall studies on equal channel angular extruded AZ31B-H24 Mg alloy with a nominal grain size of ~ 3 µm. While their grain size is similar to our material, the processing strain rate is 3 orders of magnitude lower and the grains are equiaxed with a strong basal texture along the loading direction. Yu et al. [45] performed gas-gun spall studies at higher rates on equal channel angular processed AZ31B Mg alloy with a tilted basal texture similar to the Mg alloy in this study. The grain sizes in their work also ranged between 1.5 and 5 µm. Garkushin et al. [46] performed gas-gun studies on equal channel angular pressed Ma2-1 Mg alloy with a larger average grain size at ~ 7 µm with an unreported texture. Though the alloy microstructures are different from case to case, the overall trend of rising spall strength with strain rate is nicely captured by the model (overlaid on Fig. 8). Our specimens feature a more deformed microstructure, so the potential number of cavitation sites perhaps trends higher and our spall strength data more closely follows the larger number density trend (dashed black line). We expect a better fit with the model as the µ-CT technique resolution sharpens and smaller voids are better resolved, improving both detection of the shape of the void distribution as well as the mean void spacing used in the model. Conversely, the modeling suggests that material design to improve spall failure resistance should move towards processing that introduces fewer failure nucleation sites (lower N_v) yet increases the yield strength (increase $\mathcal{R}_y$) in the microstructure. The dotted black line in Fig. 8 therefore represents the upper threshold of the microstructure design envelope for this fine-grained alloy.

We acknowledge that the simulated distribution cannot directly describe pressures above the spall strength of the material, even though the critical nucleation pressure in regions where void growth did not occur is obviously higher than the measured spall strength. Regardless, this novel approach provides an experimentally observed distribution of cavitation nucleation pressures, giving in the very least a sense of the shape of the distribution that is conventionally only reported as a single peak tensile pressure in spall experiments. Additionally, over half of the measured void radii in the raw dataset are proposed to be a combination of two or more impinged voids and 99% tend to be larger than the transitional void radius between dislocation-drag mediated and micro-inertia mediated void growth, suggesting that the growth of large voids that are responsible for spall failure is micro-inertia dominated. We intend to perform further studies on other structural metals to further evaluate our procedure.

Given the distribution of void sizes $g(a^{final})$, we can estimate the irrecoverable porosity from the distribution of voids at spall in terms of the "plastic" change in specific volume, $\Delta v_p/v_0$, when porosity is low (~ 10 percent or less [4]):

$$\frac{\Delta v_p}{v_0} = \frac{4\pi}{3} N_v \int_{a^*_{min}}^{a^*_{max}} g(a) a^3 da, \tag{9}$$

with void number density N_v. One of the simplest possible equations of state is $\Sigma = K\frac{\Delta v_e}{v_0}$, where $v = v_e + v_p$ and the recoverable change in specific volume is $\Delta v_e/v_0$ [48]. In that case the peak tension is achieved when $\dot{\Sigma} = 0$ or,

$$\dot{\Sigma} = K\left(\frac{\dot{v}}{v_0} - \frac{\Delta \dot{v}_p}{v_0}\right) = 0, \tag{10}$$

The time derivative of Eq. (9) now results in an expression relating volumetric strain rate to the time derivative of porosity at spall. Now, the subset of our void data is best approximated by the aforementioned bounded power law distribution in Eq. (3) with β=-2. After substituting this density function into Eq. (9) and taking the time derivative as per Eq. (10), the resulting expression equating the volumetric strain rate to the porosity is,

$$\frac{\dot{v}}{v_0} = \frac{4\pi}{3} N_v \frac{2}{(a^{final}_{min})^{-2} - (a^{final}_{max})^{-2}} (\dot{a}^*_{max} - \dot{a}^*_{min}), \tag{11}$$

where we have assumed that the number density N_v does not change during the loading. When Σ^* is less than $\mathcal{R}_{eos}$, the smallest void is guaranteed to not grow, so $\dot{a}^*_{min}$=0. The time derivative of Eq. (6) for the largest void under monotonically increasing tension is $\dot{a}^*_{max} = \sqrt{6/11}\sqrt{\langle \Sigma^* - \mathcal{R}_y \rangle/\rho}$ [4], so Eq. (11) can be inverted to find the spall strength as a function of the measured void distribution:

$$\Sigma^* = \mathcal{R}_y + \frac{99\rho}{384\pi^2}\left(\frac{\dot{v}}{v_0} N_v^{-1}((a^{final}_{min})^{-2} - (a^{final}_{max})^{-2})\right)^2. \tag{12}$$

Thus only the number density is required to estimate the spall strength from the final void distribution. We can again utilize the void number density from the tomography data ($N_v = 1/l^3_{nn} \sim 3.9 \times 10^{14}$ m^3). These parameters then allow us to obtain an estimate for the spall strength as 1.45 GPa. This is satisfyingly close to the spall strength measured from the velocity record (1.45 versus 1.69 GPa), but we note that

this spall strength estimate has a wide margin of deviation- the maximum and minimum void sizes and mean void spacing have large standard deviations. The analytically estimated strength is lower than the strength from the velocity record, again suggesting that the subset of voids used in Eq. (12) can be improved through better resolved tomography.

Concluding Remarks

In summary, we have introduced a methodology to learn the distribution of critical nucleation pressures for unstable cavitation in an AZ31B Mg alloy undergoing spall failure. We use micro-computed tomography scans of specimens deformed using a laser-driven shock loading apparatus that imparts incipient spall to obtain final void radius statistics. Velocimetry on the specimen free surface provides a time-resolved stress history during spall. Analytical expressions describing inertia-mediated void growth allow reverse calculation from the observed void radius statistics to the pressure distribution threshold for failure of the Mg alloy. The measured void statistics and critical pressure distributions inform a model that captures rate-dependent spall strength with satisfactory agreement to our spall experiments and those found in the literature. This technique provides the first ever experimentally reported distribution of cavitation nucleation pressures that are typically only reported as a single peak value from spall experiments. The experimentally informed analytical model in this study suggests an upper threshold in the spall strength of fine grained AZ31B Mg alloy through materials design controlling for increased yield strength and for minimized potential void nucleation sites. We expect the quality of our technique to advance as micro-computed tomography resolution improves.

Acknowledgements We thank the Dlott group at University of Illinois Urbana Champagne for their guidance in developing the laser-driven flyer apparatus used in this study, with special thanks to Dr. William Shaw, Dr. William Bassett, and Erin Nissen. We thank the Sagapuram group at Texas A&M University for providing the AZ31B target foils. Finally, we thank the Hopkins Extreme Materials Institute for their support, specifically Dr. Meng Zhao for his discussions regarding the subject matter and Dr. Amy Dagro, Matt Shaeffer, and Hao Sheng for their help with procuring materials and proofreading. This research was sponsored by the Army Research Laboratory and was accomplished under Cooperative Agreement Number W911NF-12-2-0022. The views and conclusions contained in this document are those of the authors and should not be interpreted as representing the official policies, either expressed or implied, of the Army Research Laboratory or the U.S. Government. The U.S. Government is authorized to reproduce and distribute reprints for Government purposes notwithstanding any copyright notation herein.

References

1. Antoun T, Seaman L, Curran DR, Kanel GI, Razorenov SV, Utkin AV (2003) Spall fracture. Springer, New York
2. Rinehart JS (1951) Some quantitative data bearing on the scabbing of metals under explosive attack. J Appl Phys 22(5):555–560
3. Wu XY, Ramesh KT, Wright TW (2003) The dynamic growth of a single void in a viscoplastic material under transient hydrostatic loading. J Mech Phys Solids 51(1):1–26
4. Molinari A, Wright TW (2005) A physical model for nucleation and early growth of voids in ductile materials under dynamic loading. J Mech Phys Solids 53(7):1476–1504
5. Paisley DL, Warnes RH, Kopp RA (1992) laser-driven flat plate impacts to 100 GPa with sub nanosecond pulse duration and resolution for material property studies. In: Proceedings of the APS 1991 Topical Conference on Shock Compression of Condensed Matter, pp 825–828. https://doi.org/10.1016/B978-0-444-89732-9.50189-8
6. Warnes RH, Paisley DL, Tonks DL (1996) Hugoniot and spall data from the laser-driven miniflyer. AIP Conf Proc Shock Compress Cond Matter 370(1):495–498. https://doi.org/10.1063/1.50645
7. Paisley DL, Swift DC, Johnson RP, Kopp RA, Kyrala GA (2002) Laser-launched flyer plates and direct laser shocks for dynamic material property measurements. AIP Conf Proc Shock Compress Cond Matter 2001:1343–1346. https://doi.org/10.1063/1.1483787
8. de Resseguier T, He H, Berterretche P (2005) Use of laser-accelerated foils for impact study of dynamic material behaviour. Int J Impact Eng 31(8):945–956. https://doi.org/10.1016/j.ijimpeng.2004.07.003
9. Swift DC, Niemczura JG, Paisley DL, Johnson RP, Luo S, Tierney IV TE (2005) Laser-launched flyer plates for shock physics experiments. Rev Sci Instrum 76(9):093907:1–9. https://doi.org/10.1063/1.2052593
10. Paisley DL, Luo S, Greenfield SR, Koskelo AC (2008) Laser-launched flyer plate and confined laser ablation for shock wave loading: validation and applications. Rev Sci Instrum 79(2):023902:1–8. https://doi.org/10.1063/1.2839399
11. Peralta P, DiGiacomo S, Hashemian S, Luo S, Paisley DL, Dickerson R, Loomis E, Byler D, McClellan KJ, D'Armas H (2009) Characterization of incipient spall damage in shocked copper multicrystals. Int J Damage Mech 18(4):393–413. https://doi.org/10.1177/1056789508097550
12. Wayne L, Krishnan K, DiGiacomo S, Kovvali N, Peralta P, Luo SN, Greenfield S, Byler D, Paisley DL, McClennan KJ, Koskelo A, Dickerson R (2010) Statistics of weak grain boundaries for spall damage in polycrystalline copper. Scripta Mater 63(12):1065–1068. https://doi.org/10.1016/j.scriptamat.2010.08.003
13. Brown AD, Wayne L, Pham Q, Krishnan K, Peralta P, Luo S, Patterson BM, Greenfield S, Byler D, McClellan KJ et al (2015a) Microstructural effects on damage nucleation in shock-loaded polycrystalline copper. Metall Mater Trans A 46(10):4539–4547
14. Brown AD, Pham Q, Peralta P, Luo SN, Patterson BM, Byler D, Koskelo A, Xiao X (2015) Correlations between spall damage mode preference and microstructure in shocked polycrystalline copper: a 3-d X-ray tomography study. J Dyn Behav Mater 1(4):388–396
15. Brown AD, Pham Q, Fortin EV, Peralta P, Patterson BM, Escobedo JP, Cerreta EK, Luo SN, Dennis-Koller D, Byler D et al (2017) Correlations among void shape distributions, dynamic damage mode, and loading kinetics. JOM 69(2):198–206
16. Remington TP, Hahn EN, Zhao S, Flanagan R, Mertens JCE, Sabbaghianrad S, Langdon TG, Wehrenberg CE, Maddox BR, Swift DC et al (2018) Spall strength dependence on grain size and strain rate in tantalum. Acta Mater 158:313–329

17. Krishnan K, Brown A, Wayne L, Vo J, Opie S, Lim H, Peralta P, Luo SN, Byler D, McClellan KJ, Koskelo A (2015) Three-dimensional characterization and modeling of microstructural weak links for spall damage in fcc metals. Metall Mater Trans A 46(10):4527–4538
18. Nguyen T, Luscher DJ, Wilkerson JW (2019) The role of elastic and plastic anisotropy in intergranular spall failure. Acta Mater 168:1–12
19. Grady D (2020) Statistics of energy dissipation in the hypervelocity impact shock failure transition. Int J Impact Eng 137:103435
20. Vogler TJ, Reinhart WD, Chhabildas LC (2004) Dynamic behavior of boron carbide. J Appl Phys 95(8):4173–4183
21. Mallick DD, Zhao M, Parker J, Kannan V, Bosworth BT, Sagapuram D, Foster MA, Ramesh KT (2019a) Laser-driven flyers and nanosecond-resolved velocimetry for spall studies in thin films. Exp Mech 59:611–628
22. Mallick DD, Williams CL, Wilkerson JW (2020) A brief review of spall failure in pure and alloyed magnesium. Dyn Behav Mater 46(10):4539–4547
23. Jones TL, DeLorme RD, Burkins MS, Gooch WA (2007) Ballistic evaluation of magnesium alloy az31b. Technical report, ARMY RESEARCH LAB ABERDEEN PROVING GROUND MD
24. Sagapuram D, Efe M, Moscoso W, Chandrasekar S, Trumble KP (2013) Controlling texture in magnesium alloy sheet by shear-based deformation processing. Acta Mater 61(18):6843–6856
25. Mallick DD, Zhao M, Bosworth BT, Schuster BE, Foster MA, Ramesh KT (2019b) A simple dual-beam time-multiplexed photon doppler velocimeter for pressure-shear plate impact experiments. Exp Mech 59(1):41–49
26. Mallick DD (2019) Shock-induced failure of protection materials using laser-driven micro-flyers. PhD thesis, Johns Hopkins University
27. Bassett WP, Johnson BP, Salvati III L, Nissen EJ, Bhowmick M, Dlott DD (2020) Shock initiation microscopy with high time and space resolution. Propellants Explos Pyrotech 45(2):223–235
28. Shazly M, Prakash V (2008) Shock response of a gamma titanium aluminide. J Appl Phys 104(8):083513
29. Ek DR, Asay JR (1986) The stress and strain-rate dependence of spall strength in two aluminum alloys. Shock waves in condensed matter. Springer, New York, pp 413–418
30. Bless SJ (1981) Spall criteria for several metals. Technical report, DAYTON UNIV OH RESEARCH INST
31. Appleby-Thomas GJ, Hazell PJ (2010) A study on the strength of an armour-grade aluminum under high strain-rate loading. J Appl Phys 107(12):123508
32. Selvarajou B, Joshi SP, Benzerga AA (2019) Void growth and coalescence in hexagonal close packed crystals. J Mech Phys Solids 125:198–224
33. Patterson BM, Escobedo-Diaz JP, Dennis-Koller D, Cerreta E (2012) Dimensional quantification of embedded voids or objects in three dimensions using X-ray tomography. Microsc Microanal 18(2):390–398
34. Huang Y, Hutchinson JW, Tvergaard V (1991) Cavitation instabilities in elastic-plastic solids. J Mech Phys Solids 39(2):223–241
35. Ghosh S, Cheng J (2018) Adaptive multi-time-domain subcycling for crystal plasticity fe modeling of discrete twin evolution. Comput Mech 61(1–2):33–54
36. Wright TW, Ramesh KT (2008) Dynamic void nucleation and growth in solids: a self-consistent statistical theory. J Mech Phys Solids 56(2):336–359
37. Wilkerson JW, Ramesh KT (2014) A dynamic void growth model governed by dislocation kinetics. J Mech Phys Solids 70:262–280
38. Wilkerson JW (2017) On the micromechanics of void dynamics at extreme rates. Int J Plast 95:21–42
39. Wang Y, Choo H (2014) Influence of texture on hall-petch relationships in an mg alloy. Acta Mater 81:83–97
40. Lloyd JT, Williams CL, Clayton JD (2020) Dynamic strength of az31b-4e and amx602 magnesium alloys under shock loading. J Dyn Behav Mater 1:11. https://doi.org/10.1007/s40870-019-00230-x
41. Farbaniec L, Williams CL, Kecskes L, Ramesh KT, Becker R (2016) Microstructural effects on the spall properties of ecae-processed az31b magnesium alloy. Int J Impact Eng 98:34–41
42. Wilkerson JW, Ramesh KT (2016) Unraveling the anomalous grain size dependence of cavitation. Phys Rev Lett 117(21):215503
43. Marsh SP (1980) LASL shock Hugoniot data, vol 5. University of California Press, Berkeley
44. Trojanová Z, Lukáč P, Podrábskỳ T, Pešička J (2011) High strain rate behaviour of an az31+ 0.5 ca magnesium alloy. Materials Engineering-Materiálové inžinierstvo (MEMI) 19(1):12–17
45. Xia Y, Li T, Li L, Liu S, Li Y (2017) Influence of initial texture on the shock property and spall behavior of magnesium alloy az31b. Mater Sci Eng A 700:259–268
46. Garkushin GV, Razorenov SV, Krasnoveikin VA, Kozulin AA, Skripnyak VA (2015) Effect of structural factors on mechanical properties of the magnesium alloy ma2-1 under quasi-static and high strain rate deformation conditions. Phys Solid State 57(2):337–343
47. Thao Nguyen, Luscher DJ, Wilkerson JW (2020) A physics-based model and simple scaling law to predict the pressure dependence of single crystal spall strength. J Mech Phys Solids 137:103875
48. Czarnota C, Jacques N, Mercier S, Molinari A (2008) Modelling of dynamic ductile fracture and application to the simulation of plate impact tests on tantalum. J Mech Phys Solids 56(4):1624–1650